scientific reports

Check for updates

OPEN

Case studies of different types of precipitation at Ny-Ålesund, Arctic

Lekhraj Saini[1], Saurabh Das[1]✉ & Nuncio Murukesh[1,2]

Arctic precipitation plays a crucial role in shaping the surface mass balance of Arctic sea ice and has wide-ranging impacts on local climate, ecosystems, and global sea level dynamics. With the Arctic undergoing warming trends, historical data and climate models indicate a shift from primarily snowfall to a rise in liquid and mixed forms of precipitation. This study tried to explain the microphysical characteristics and atmospheric conditions associated with different forms of precipitation and their transitions. The phase changes were explained by the vertical precipitation profiles over Ny-Ålesund, Svalbard (78^o 55′ N, 11^o 56′ E), observed using a Micro Rain Radar (MRR) and vertical atmospheric profiles using the ground-based microwave radiometer (MWR). Atmospheric conditions were also analysed based on ERA5 reanalysis data at different pressure levels. For the cases studied here, it was found that the southerly warm-moist air mass plays a crucial role in the change of precipitation phase and intensity. Warm and moist winds at $\sim$ 2-3 *km* altitude facilitated high temperature and moisture that helped snow to melt in liquid, resulted in rainfall over the location. Additionally, hourly winds from ERA5 reanalysis indicated upward wind motion was responsible for the formation of graupel. The insight gained from this study will be useful to predict the further precipitation trend over the Arctic more accurately.

The Arctic region exhibits an exceptional sensitivity to climate change, surpassing that of any other area on the Earth[1]. Over the past century, the Arctic has experienced a warming rate nearly twice the global average[2]. These changes are closely linked to the rise in greenhouse gases, leading to higher temperatures, ice melting, shifts in storm patterns, and changes in timing and types of precipitation[3,4]. The reduction in sea ice are intricately linked with the increase in Arctic precipitation. Arctic displays a substantially higher mean precipitation sensitivity (4.5 percent increase per degree of temperature warming) in contrast to the global average (1.6 to 1.9 percent per kelvin)[5]. Rainfall events have become more frequent and intense due to rapid Arctic warming, triggering snow and ice melting by reducing albedo and releasing latent heat[6].

Precipitation is a pivotal element of the hydrological cycle in polar regions, which predominantly falls in the form of snow, but as the region warms, there is a potential for shifts in precipitation patterns, leading to a greater occurrence of rain and a mixture of rain and snow[7]. Precipitation analysis during 1993-2020 found significant positive trends in rainfall (0.87 *mm* especially in winter (0.36 *mm*/decade) and fall (0.79 *mm*/decade) exceeding the mean precipitation trend[8].

Both local and global variables affect Arctic warming, and increased moisture leads to more precipitation with enhanced rainfall. These changes are linked to tropospheric temperature and moisture trends rather than surface temperature and humidity increases[8–10]. However, the precise impact of these factors on the transition between different phases and intensities of precipitation at daily and sub-daily scales remains poorly understood. The vertical profile of precipitation well explains these processes with different altitude levels. The importance of understanding the vertical profile of precipitation and associated atmospheric conditions is highlighted in tropical regions, which also helps in accurate quantitative precipitation estimation through ground and space-borne radars[11,12]. The role of vertical profiles on climatological patterns and precipitation processes in remote polar regions like Antarctica were also studied[13,14]. In this context, ground-based in-situ vertical profilers offer a distinct advantage over satellite measurements by providing more detailed monitoring capabilities in the proximity of the Earth's surface. These studies underscore the need for a deeper understanding of the vertical structure of precipitation and associated atmospheric conditions in the Arctic region.

The present study focuses on Ny-Ålesund, Svalbard (74^o-81^o N), positioned in the primary pathway for atmospheric energy transport into the Arctic[15]. Ny-Ålesund experiences relatively high tropospheric temperatures[16,17] and a coastal Arctic climate[18], with an average annual precipitation of around 461 mm[19]. The North Atlantic Arctic is a region highly affected by climate change, characterized by warming, sea ice loss, and changes in circulation patterns[20,21]. In recent years, the region has witnessed increased cloudiness, precipitation,

[1]Present address: Department of Astronomy, Astrophysics and Space Engineering, Indian Institute of Technology Indore, Indore, Madhya Pradesh 453552, India. [2]National Centre for Polar and Ocean Research, Ministry of Earth Sciences, Goa 403804, India. ✉email: das.saurabh01@gmail.com; saurabh.das@iiti.ac.in

and cyclone activity, especially in winter[22–25]. During south and southwest air mass advection, the region often experiences increased cloudiness, stronger winds, higher temperatures, elevated humidity, and heavier precipitation, particularly in West Spitsbergen[26]. Indian research station 'Himadri' in Ny-Ålesund, Arctic, facilitates in-situ precipitation observation utilizing a Micro Rain Radar (MRR) as a vertical precipitation profiler in conjunction with a disdrometer for ground-level precipitation measurements. Additionally, a ceilometer is employed for monitoring cloud base height, while a microwave radiometer (MWR) is utilized for assessing the vertical atmospheric profiles such as temperature and humidity.

The present study is driven by two primary objectives. The initial aim pertains to examining the vertical structure of reflectivity (Ze) in various forms of surface precipitation observed in the Arctic region. The second objective focuses on investigating the atmospheric conditions and moisture pathways, both vertically and spatially, that are linked to these distinct forms of precipitation and their transition. This study used ground-based instruments, which is critical due to the region's unique climate sensitivity and the scarcity of reliable observations. In-situ observations provide valuable information on vertical structures of precipitation, which are crucial for understanding precipitation processes in the Arctic. This study advances the scientific knowledge by addressing challenges in distinguishing precipitation types and offering a better understanding of events influenced by atmospheric conditions. Furthermore, these observations will enhance the evaluation of satellite-based and reanalysis precipitation datasets and contribute to improved climate and weather models. The present study is expected to make a significant contribution in understanding the impacts of climate change feedback on precipitation patterns in the Arctic region.

Data and methods

Site location

In situ observation data were gathered from the Himadri Research Station, a coastal site in the Arctic. The base is located in Ny-Ålesund (78^o 55' N, 11^o 56' E), Svalbard, Norway, as shown in Figure 1. This is located on the southern shore of Kongsfjorden, one of the many deep and wide fjords on Spitsbergen's west coast. Due to its position, its atmosphere is mostly influenced by the nearby orographic features and the warm ocean's diabatic heating[17]. All the instruments are maintained by the National Center for Polar and Ocean Research (NCPOR), India, and operate on the roof of the Gruvabadat Atmospheric Laboratory (GAL) at 40 m above sea level, as shown in Figure 2.

Data and instruments

For this study, several precipitation events from 2018 to 2022 were analysed, and three representative events are presented here to understand the complexities of Arctic weather. The events presented are: snowfall with graupel (December 14^{th}-16^{th}, 2018), the transition between rain and snow observed in summer (June 7^{th}-8^{th}, 2020) and in winter (November 14^{th}-16^{th}, 2020). Surface level meteorological parameters, such as averaged temperature at $2m$ level, relative humidity, mean wind speed, and direction for $1-hour$ temporal resolution, collected by MET-Norway (from a nearby station)[28]. To complement detailed local observations, air-mass trajectories, temperature, and moisture profiles were analyzed using ERA5 reanalysis data[29] and HYSPLIT back-trajectory simulations[30]. Hourly averaged ERA5 datasets, the latest reanalysis from the European Centre for Medium-Range Weather Forecasts (ECMWF), were utilized for various pressure levels (1000-225 hPa) and the spatiotemporal distribution within the region of $0-60^o$ E and $60-90^o$ N. Atmospheric conditions such as temperature, U and V components of wind, vertical velocity, specific humidity, and relative humidity were analysed from the ERA5 dataset. Ground-based instruments were used for in-situ observation and are summarised next.

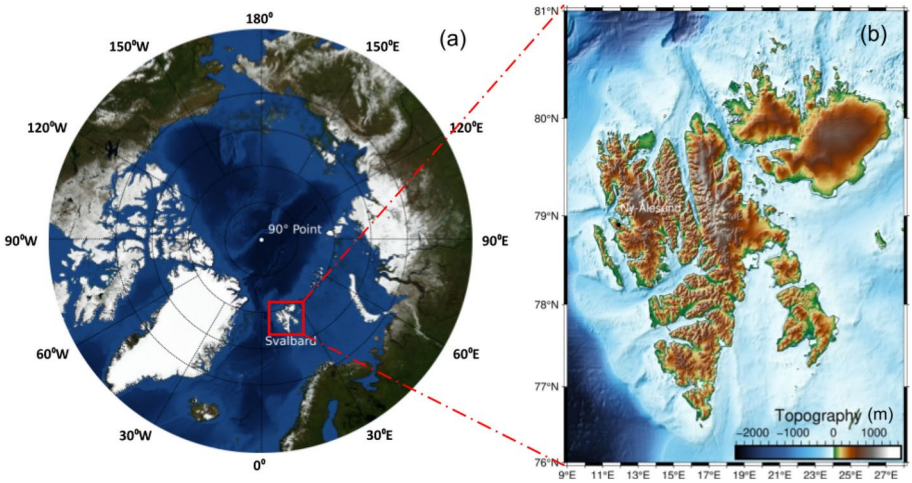

Fig. 1. Geographical location (a) and topographic map (b) of Svalbard, with a black dot marking the Ny-Ålesund research station. The figure was created using Basemap 1.4.1 (Matplotlib)[27] for the polar map and PyGMT 0.13.0 (Generic Mapping Tools) for the study location.

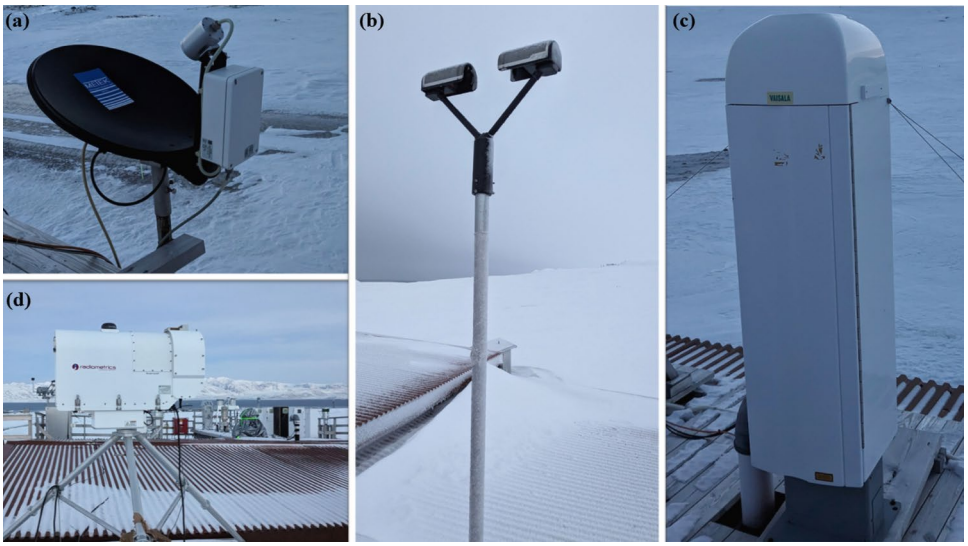

Fig. 2. In-situ ground-based instruments (a) micro rain radar (MRR) (b) OTT $\mathrm{parsivel}^2$ disdrometer (c) laser ceilometer LIDAR (d) microwave radiometer (MWR) operating at Gruvabadat Atmospheric Laboratory in Ny-Ålesund, svalbard (image: Indian-Arctic winter expedition 2023-24).

Micro rain radar (MRR)
The FM-CW (frequency modulated continuous wave) profiling MRR by METEK GmbH used in this study is shown in Figure 2(a). It operates at a transmit frequency of 24 GHz (λ = 1.24 *cm*) in the K band and produces 64-bin Doppler power spectra spanning a vertical range of 32 bins. It was operated with a temporal resolution of 1 minute and a vertical resolution of 50 *m* (during 2018-19) and 200 *m* (during 2020-till date). It has a parabolic dish with a 0.5-meter effective aperture diameter fixed at a 63^o angle with the vertical axis. Two of its major limitations are the capacity to distinguish between snow and liquid particles and the presence of snow and ice on the radar antenna. For snow and ice retrieval, instead of the original MRR software, the developed algorithm ImProToo has been used in this present study[31]. For the second limitation, to avoid snow accumulation on the dish, a 200 W dish heating system has been installed.

OTT parsivel disdrometer
The **Par**ticle **Si**ze and **Vel**ocity ($\mathrm{ParSiVel}^2$) optical disdrometer shown in Figure 2(b), manufactured by OTT Hydromet GmbH, plays a crucial role in monitoring hydrometeor sizes, types, and fall velocities at ground level. This instrument monitors the hydrometeor sizes and fall velocities as they cross the 1 *mm* horizontal laser beam of 780 *nm* with an area of 180 $\times$ 30 mm^2 between the disdrometer's transmitter and receiver heads. This measures hydrometeor with diameters of 0-25 *mm* and velocities of 0-22.4 ms^{-1} in 32 classes bins[32,33]. OTT classifies the precipitation based on the particle size and the vertical velocities of hydrometeors[32]. However, it's important to note that they have certain limitations, particularly in windy conditions and when dealing with closely spaced precipitation particles. This instrument has been in operation since 2018 at GAL.

Ceilometer
A Vaisala CL51 laser ceilometer is being operated at the GAL for the purpose of ascertaining the cloud base height. Utilizing LIDAR (light detection and ranging) technology, the device determines the cloud base height (CBH). A pulsed laser beam transmitted vertically into the atmosphere interacts with air molecules and particles, generating the cloud backscatter coefficient (BSC) using the algorithm provided by Vaisala[34]. Operating at a principal wavelength of 910 *nm*, it can measure CBH at distances of up to 15 *km*. The vertical and temporal resolutions are established at 10 *m* and 6 *s* respectively. In the case of the CL51, if the lower cloud layer is translucent enough to permit the backscatter light from the upper cloud layer, it becomes feasible to identify up to three cloud layers[35]. The instrument is in operation since spring 2015.

Microwave radiometer (MWR)
A MWR, MP-3000A, manufactured by Radiometrics, provides vertical profiles of temperature and humidity up to a height of 10 *km* and low-resolution cloud liquid water content[36,37]. The radiometric profiler detects brightness temperature at 12 frequencies within the microwave spectrum, primarily influenced by atmospheric water vapour, cloud liquid water, and molecular oxygen emissions[38,39]. The radiometer observes within an inverted cone, featuring a 2-3 degree beamwidth at 51-59 GHz and a 5-6 degree beamwidth at 22-30 GHz. The radiometric profiler also includes zenith infrared sensors and surface temperature, humidity, and pressure sensors. It continuously measures temperature and humidity profiles up to 10 *km* with high vertical resolution that decreases with altitude (ranging from 0.05 *km* to 0.5 *km* with 58 range gates). Here vertical atmospheric profiles used up to 5 *km* heights for 2018 and 10 *km* for the year 2020 case studies with a temporal resolution of 1-5 minutes.

Methodology

The substantial variability in snow particle shapes and densities alters the size-fall velocity (W) relationship, introducing significant uncertainty in snow rate estimation. As already mentioned, the originally produced averaged data from the MRR software lacked sensitivity for snowfall estimation using remote sensing techniques[40]. To overcome this limitation, the processing tool IMProToo (Improved MRR Processing Tool) method[31]. This method incorporates signal and noise processing techniques, featuring a dynamic de-aliasing routine that allows to make observations even when the nyquist velocity range is exceeded. Additionally, it includes noise removal based on identifying the most prominent peak. IMProToo processes the raw file from MRR and produces the output particularly well suited for snow studies. Hence, instead of snow rate or size distribution, equivalent reflectivity factor (Ze) and fall velocity (W) from the IMProToo processed file used in this study. The contour frequency by altitude diagram (CFAD) of these parameters is used to explain the precipitation microphysical evolution with different altitude levels.

In 32 range gates, the initial one (range gate no. 0) corresponding to the lowest height is excluded from processing for quality control. Following this, the subsequent two range gates (no. 1 and 2) with the last range gate (no. 31) are also omitted from analysis due to near-field/excessive noise effects. Consequently, there are 28 exploitable range gates remaining, resulting in an observable height range spanning from 300 to 6000 *m* depending on the height resolution. In this context, parsivel^2 plays a crucial role by assisting in the study of ground precipitation and distinguishing between various precipitation types. Hence, observations from OTT parsivel^2 were used to classify the MRR profiles in separate precipitation regimes as per WMO guidelines[41]. Ceilometer data for CBH were averaged for 1 *minute* temporal resolution from 6 *second* temporal resolution.

Near-surface meteorology parameters at study location such as temperature, humidity, winds from MET-Norway were also used. The vertical profile of atmospheric conditions was derived from both ground-based MWR (level 2) and ERA5 hourly reanalysis data. To better understand the synoptic conditions and their spatio-temporal distribution analyses were conducted at different atmospheric pressure levels. It was highlighted that the 500 *hPa* and 850 *hPa* levels are critical for divergence and advection, respectively[42]. Therefore, temperature and moisture advection at the 850 *hPa* level, divergence at the 500 *hPa* level, mean sea level pressure (MSL), and 2 m temperature were analyzed. Based on the temperature and moisture vertical profiles over the study location, moisture pathways were effectively analyzed using the spatio-temporal distribution of temperature, moisture and winds at different pressure levels for each event. Below are the equations used to calculate the advection of temperature and moisture, while divergence data were obtained directly from ERA5.

$$\text{Temperature Advection} = -\left(\frac{\partial T}{\partial x}\cdot u_{\text{wind}} + \frac{\partial T}{\partial y}\cdot v_{\text{wind}}\right) \tag{1}$$

$$\text{Moisture Advection} = -\left(\frac{\partial q}{\partial x}\cdot u_{\text{wind}} + \frac{\partial q}{\partial y}\cdot v_{\text{wind}}\right) \tag{2}$$

Here T, q, u_{wind} and v_{wind} represent the temperature, specific humidity, *u* and *v* components of horizontal winds respectively.

Results

Climatology of the study location

The monthly averaged surface temperature over the Ny-Ålesund shows significant seasonal variations based on the dataset from 2011-2022[28]. The mean temperature ranges from ∼-13 $\pm 4^{o}C$(March) to ∼5 $\pm 1^{o}C$ (July), with a daily minimum of ∼ -25 $\pm 5^{o}C$ in the coldest month of March and a daily maximum of ∼ 15 $\pm 4^{o}C$ in the warmest month of July, as shown in Figure 3(a). Figure 3(b) displays the monthly fraction of precipitation

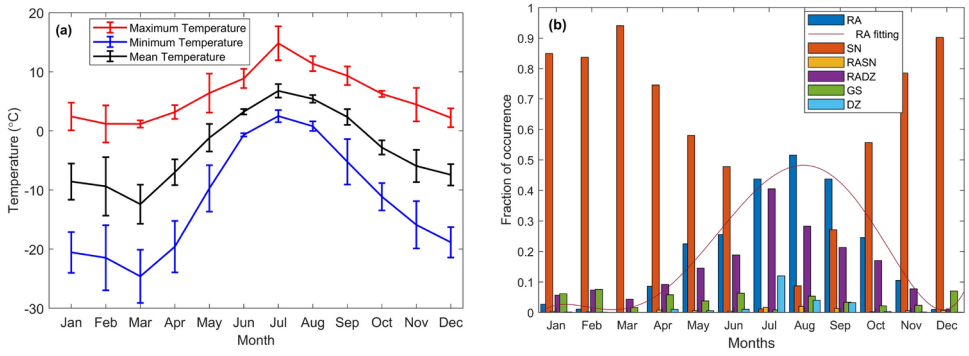

Fig. 3. (a) Averaged monthly surface temperature variation at Ny-Ålesund[28] and (b) Fraction of occurrence of different precipitation type during 2018-21, with 5th polynomial fitting for rain (RA) from parsivel^2 disdrometer during 2018-21.

contributed by each form. This highlights snow as a significant component of the total precipitation, followed by rain, rain with drizzle, drizzle, graupel and rain mixed with snow. The occurrence of rain increases with rising temperatures, as seen from distribution. During the summer season, when sunlight is abundant in the Arctic atmosphere (midnight sun), rain reaches its peak occurrence, while snow occurrences decrease substantially. A study analysing CBH from April 2015-October 2017 shows that CBH1 in summer is at approximately 1.2 *km*, the lowest among all seasons (1.8 *km* in autumn, 2.3 *km* in winter, and 1.5 *km* in spring)[43]. Furthermore, the maximum detection of CBH2 and CBH3 occurs during summer, suggesting thinner low-level clouds compared to other seasons in Ny-Ålesund. Over 80% of summer clouds are identified as low-level clouds, which have significant radiative effects that led to the warming of the surface[44,45]. This aligns rain frequency directly with the annual temperature and cloud patterns observed in the region.

To understand the microphysics and atmospheric conditions associated with different forms of Arctic precipitation, data from 2018 to 2022 has been analysed. Based on that, three key representative events were selected to closely examine the Arctic precipitation, which are discussed here.

Case studies

Precipitation as graupel with snow

The first precipitation event, including snow and graupel/small hail (GS), a type of precipitation characterized by soft, white ice pellets, was selected for the study from December 14^{th}-16^{th} in 2018, as presented in Figure 4(a-b). The precipitation event started with snowfall on 14^{th} at 19:00 *UTC*, followed by the emergence of graupel (red dots) at approximately 3:30 *UTC* and persisted for over $10-hour$ (Figure 4(d)). Later followed by high-intensity snowfall, accompanied by hail. To investigate these changes, the vertical profiles of the BSC and CBH, MRR-driven Ze and W were examined, as presented in Figure 4(a-c). Observation of BSC in Figure 4(a) indicates cloud cover below 1 *km* with corresponding CBH shown in Figure 4(b). Since both snow and graupel are solid forms of precipitation, no significant variation in the vertical profiles of reflectivity and fall velocity was observed between these phases. However, as expected high fall velocity was observed during GS, indicating that hail falls faster than snow.

At ground level, the temperature and relative humidity variations correlate with each other (Figure 4(e)). During the snow period, the temperature remains below freezing level, while it crosses during the graupel period, accompanied by an increase in relative humidity. Subsequently, both temperature and relative humidity decreased during the later part of snowfall. During the graupel southwesterly winds with low speed (< 2 ms^{-1}) were observed, whereas northwesterly winds with high speed (> 10 ms^{-1}) observed during snow, as presented in (Figure 4(f)).

In Figure 5 vertical profile of various atmospheric parameters from MWR and ERA5 is presented to show the correlation between ground-based and global reanalysis datasets. Vertical atmospheric profiles for snow to graupel transition with the MWR observation shown in Figure 5(b-e) with MRR reflectivity in Figure 5(a). It was observed that when snowfall started at 19:00 *UTC* on December 14^{th}, the temperature was below freezing level, accompanied by a moderate vapour density as shown in Figure 5(b-c). Initially, the liquid water density profile exhibited some low-level cloud liquid content around 1 *km* Figure 5(d). As time progressed, both the temperature and vapour density began to enhance near the surface.

During graupel, the near surface temperature reaches near freezing level, accompanied by a vapour density exceeding 4 gm^{-3}. High liquid water density can be seen in Figure 5(c) between 1-3 *km* with below freezing level

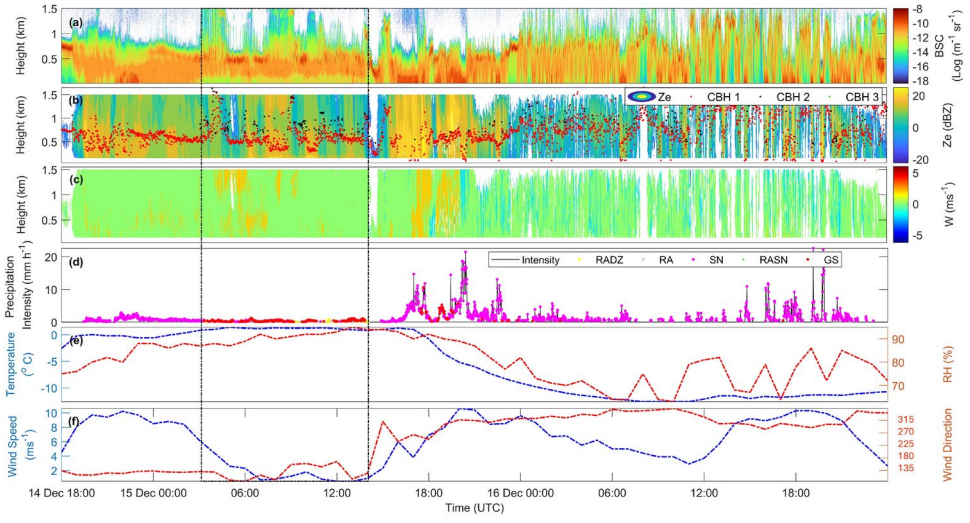

Fig. 4. Time series of vertical profiles: (a) BSC, (b) reflectivity (Ze) with CBH1 (red), CBH2 (blue), and CBH3 (green), (c) fall velocity (W) observed by ceilometer and MRR, respectively. Ground observations include (d) precipitation intensity from the disdrometer showing transitions from snow (SN, magenta) to graupel (GS, red) and vice versa; (e) 2*m* temperature (blue dashed) and relative humidity (red dashed); and (f) mean wind speed (blue dashed) and wind direction (red dashed) during December 14^{th} - 16^{th} 2018.

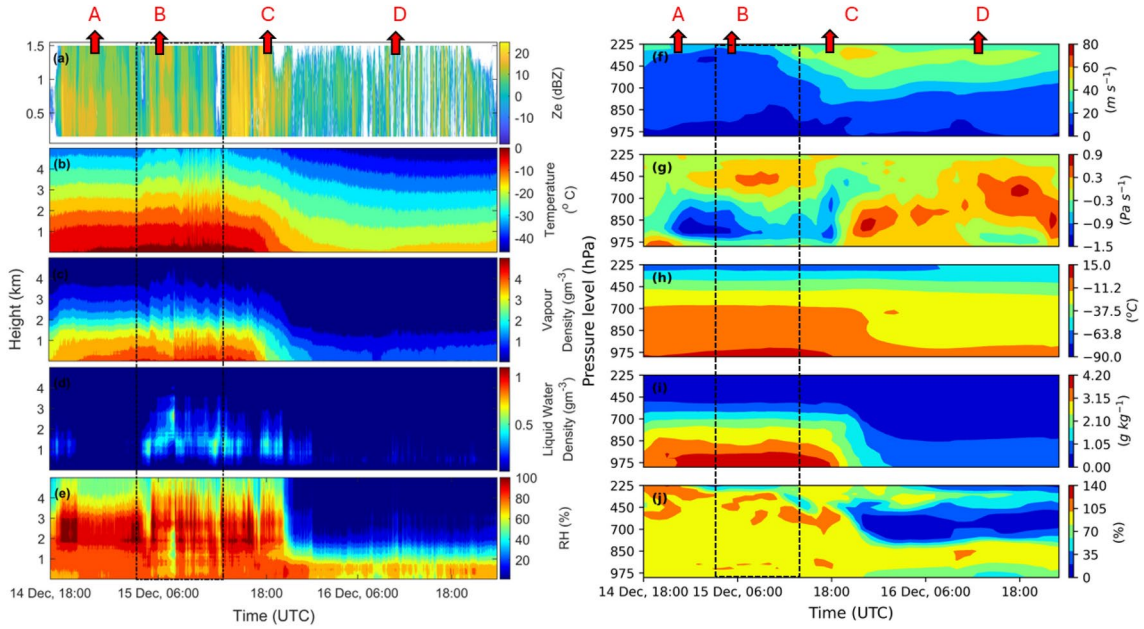

Fig. 5. Time series of (a) reflectivity (Ze) along with corresponding vertical atmospheric sounding from ground-based vertical profiler MWR: (b) temperature (^oC), (c) vapour density (gm^{-3}), (d) liquid water content (gm^{-3}), and (e) relative humidity (%). Vertical profile of atmospheric conditions based on ERA5 hourly reanalysis data: (f) horizontal wind speed (g) vertical velocity (h) temperature (^oC), (i) specific humidity (gkg^{-1}), and (j) relative humidity (%) during December $14^{th} - 16^{th}$, 2018.

temperature ($> -20^oC$) which indicates the presence of supercooled water[46–48]. Since the CBH from Figure 4(a) is mostly below 1 *km*, it indicates the availability of supercooled water within the cloud. This type of cloud is referred to as a mix-phased cloud[45,49–52]. These conditions persisted even after the graupel event until 20:00 *UTC* on December 15^{th}. These post-graupel conditions were associated with high-intensity snowfall with hail[53]. On December 16^{th}, conditions were characterized by a lower temperature, vapour density, and liquid content in comparison to the previous day. Relative humidity was higher before and in December 15^{th} compared to the later part of December 16^{th} Figure 5(e) which resulted in low-intensity snowfall as shown in Figure 4(d)[54].

Delving deeper into the atmospheric conditions shown in Figure 5(f-j) using ERA5 reanalysis data, low-speed horizontal winds were observed at lower altitudes below 700 *hPa* Figure 5(f). An important aspect to note here is the vertical wind velocity in Figure 5(g). During the snow to graupel transition, upward velocity was observed from the surface up to $\sim$ 700 *hPa* and downward motion above that. The temperature profile also exhibits near-surface enhancement during the graupel, coinciding with an increase in moisture as specific humidity as shown in Figure 5(h-i). This result is consistent with the MWR atmospheric profiles, ERA5 presents similarities in the temperature and specific humidity profiles. The good agreement as seen between these two datasets also present an opportunity to use the reanalysis data to understand the spatio-temporal distribution of atmospheric parameters.

Synoptic conditions from ERA5 reanalysis data on a large scale can be observed in Figure 6 for snow, graupel, and their transition. Four time instants: A, B, C, and D, as mentioned in Figure 5, correspond to 20:00 *UTC* on December 14^{th}, 06:00 *UTC* on December 15^{th}, 18:00 *UTC* on December 15^{th}, and 12:00 *UTC* on December 16^{th} respectively, were suited for detailed analysis. Figure 6 shows the mean surface-level pressure with $2m$ surface temperature as contour lines in column 1^{st}, the advection of temperature and moisture at the 850 *hPa* pressure level in columns 2^{nd} and 3^{rd}, respectively, and the 4^{th} column represents the 500 *hPa* level divergence. A distinct low-pressure system is centered to the north-west of Svalbard, whereas a high-pressure system was observed to the south of Svalbard at mid-latitude during the initial snowfall phase in time instant A in Figure 6(A). This led to a southwesterly cold wind at 850 *hPa* level and was associated with negative advection of temperature as well as moisture. The $24-hour$ back-trajectory analysis using HYSPLIT also supports the same as shown in Figure S1, in the supporting file. The 500 *hPa* level convergence may have been created due to the reduced speed of horizontal winds near 500 *hPa* level over the study location. This convergence leads a small downward motion upto 700 *hPa* in atmosphere observed from Figure 5(g).

The low pressure system at time instant B in Figure 6(B) during graupel precipitation, centered to the north part of Svalbard. This led to a southwesterly low-level wind to converge at the study location and create an upward motion of winds observed during the graupel up to 700 *hPa* level, also shown in Figure 5(g). Upward motion led to instability in the atmospheric column, which increased the random motion of supercool water and ice crystals to form granule via the collision that subsequently become frozen on the ice surface through a process called riming.[55–60].

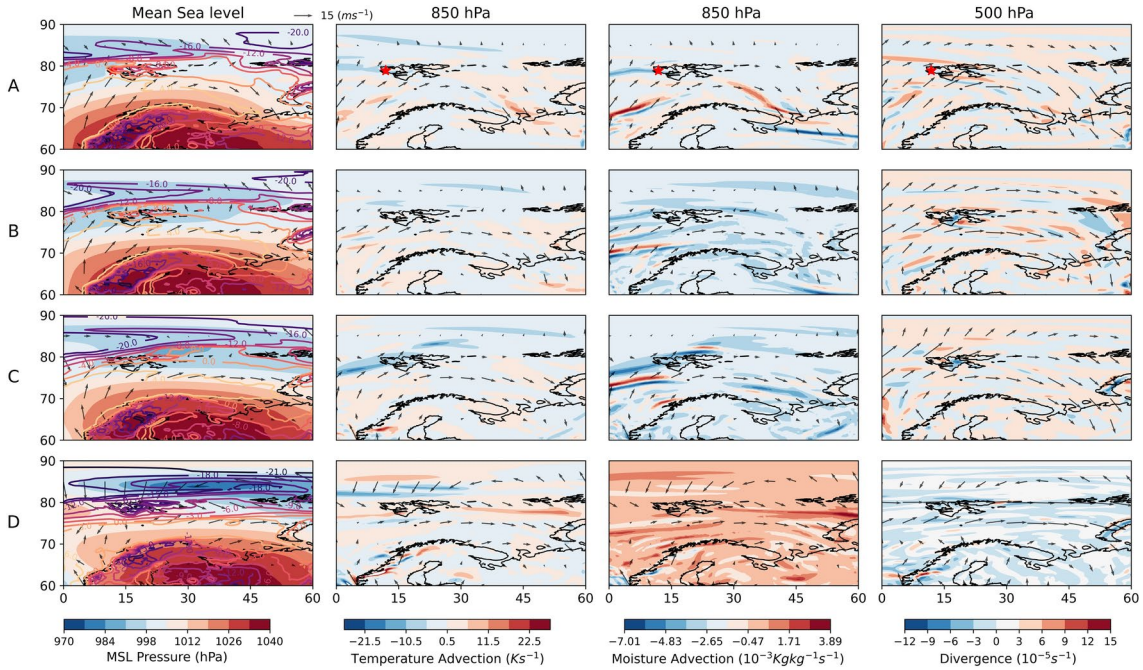

Fig. 6. Synoptic chart of MSL pressure with 2*m* level temperature contour line (column 1^{st}), temperature advection at 850 *hPa* level (column 2^{nd}), moisture advection at 850 *hPa* level (column 3^{rd}) and divergence at 500 *hPa* level (column 4^{th}) at four time instants during December $14^{th} - 16^{th}$, 2018 in rows: (A) 20:00 *UTC*, December 14^{th}; (B) 06:00 *UTC*, December 15^{th}; (C) 18:00 *UTC*, December 15^{th}; and (D) 12:00 *UTC*, December 16^{th}.

At time C in Figure 6(C) when the graupel event transforming into a snow event, the low-pressure system moved north of Svalbard. However, the study site was still at low pressure and associated with small upward wind motion. This shift of pressure system brings westerly cold winds that led to reduced temperature and moisture advection at 850 *hPa* level. Synoptic conditions were similar to graupel event, as it experienced high intensity snowfall with hail[53].

The last time instant D in Figure 6(D) is during the end of the event with snowfall. The low-pressure system shifts to the north-east of Svalbard, and the study location experiences high pressure compared to other instants of this event. This change in pressure led to divergence at locations associated with northwesterly circular wind flow and a small downward wind motion observed at near surface level. The HYSPLIT back-trajectory analysis also confirms the wind pattern, downward and upward motion (see Figure S1 in the supporting files).

To understand the moisture pathways for the event at the near surface level, spatio-temporal analysis of temperature and moisture at the 900 *hPa* level is shown in Figure 7. Figure 7(t-r) shows the temperature (t), vertical winds (w), specific humidity (q) and relative humidity (r) at the time instant A-D as defined earlier. When snowfall starts at time instant A, low-speed winds ($\leq$20 ms^{-1}) originating from the southwest direction reach over the location site (Figure 7(A)). These winds have below freezing level temperatures and moderate moisture levels, resulting in high relative humidity and favorable conditions for snowfall. As time progresses, the wind speeds increase, but the temperatures and moisture content decrease, leading to similar relative humidity levels (Figure 7(B)). At the last instant in Figure 7(D), very low temperatures influenced by northwesterly moderate winds with low moisture levels favor low intensity of snowfall.

The CFAD of reflectivity (Ze) for both types of precipitation, graupel and snow, presented in Figure 8, shows similar trends across height. The majority of precipitation particles in both cases fall within the range of 10-20 *dBZ*. However, graupel mostly remains under 20 *dBZ*, while snow surpasses this level, extending to approximately 25 *dBZ* and exhibiting a broader range of approximately 0-25 *dBZ*. The reflectivity behavior of snow mirrors that of the first case study below 1.5 *km*, where it intensifies as the particles descend towards the ground. Meanwhile, graupel follows a consistent pattern, with minor fluctuations evident around the altitude of 1 *km*. In fall velocity, snow shows a broader range, 0-2 ms^{-1} while the majority of graupel falls above 1 ms^{-1}. This clearly shows that graupel falls faster with a narrow range and high reflectivity compared to SN.

Rain and snow in summer

The second case study was based on the snow-rain event that occurred during summer in June 7^{th} - 8^{th}, 2020. Figure 9(d) highlights the different precipitation types at ground with phase transition represented by black dotted lines. The first period, referred to as "Snow event-1", was characterized predominantly by snowfall observed at the ground from 00:00 to 12:00 *UTC* on June 7^{th}. The subsequent period, spanning from 12:00 on June 7^{th} to 05:00 *UTC* on June 8^{th}, was characterized as a "Rain event" indicating a shift towards liquid precipitation. Finally, the last period, from 05:00 to 24:00 *UTC* on June 8^{th}, displayed a return to snowfall

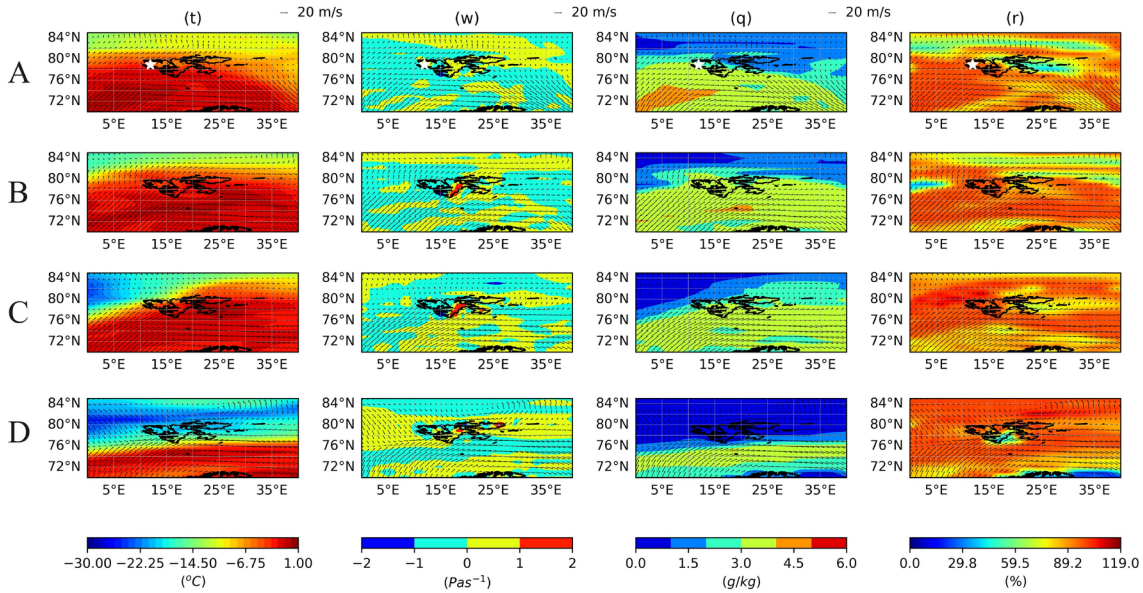

Fig. 7. Spatio-temporal of atmospheric variable with horizontal wind speed vectors at the 900 *hPa* pressure level at four time instants during December $14^{th} - 16^{th}$, 2018 in rows: (A) 20:00 *UTC*, December 14^{th}; (B) 06:00 *UTC*, December 15^{th}; (C) 18:00 *UTC*, December 15^{th}; and (D) 12:00 *UTC*, December 16^{th}.

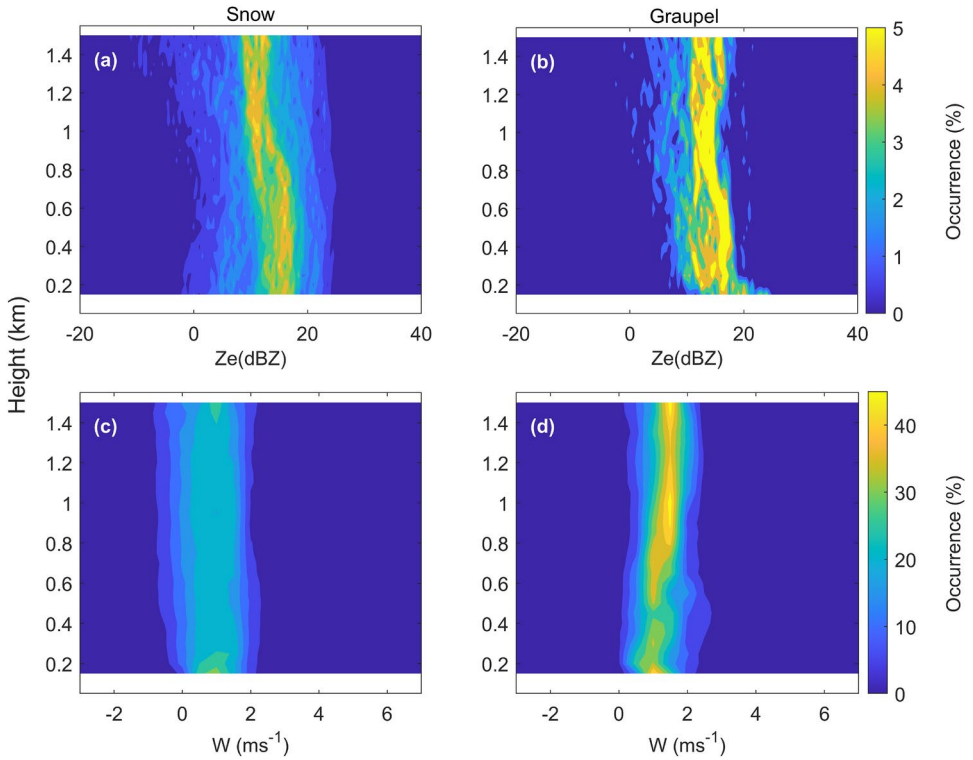

Fig. 8. Normalized (CFAD) for (a-b) reflectivity (Ze) and (c-d) fall velocity (W) for snow and graupel respectively for December $14^{th} - 16^{th}$, 2018.

dominance, labeled as "Snow event-2". Both BSC and CBH extended up to 4 *km* before the onset of precipitation, then descended below 2 *km* as snowfall began as shown in Figure 9(a-b). During "Snow event-1," the radar reflectivity and fall velocity profiles were uniform up to 6 *km*. During the "Rain event", CBH moved downward, reaching near the surface below 0.5 *km*. Enhancement in Reflectivity with fall velocity below ~ 2 *km* observed during rain as shown in Figure 9(b-c). This can be explained by the increase in the dielectric constant caused by the water coating on ice crystals as snowflakes melt[61–63]. This layer was identified as the melting layer at $\sim$

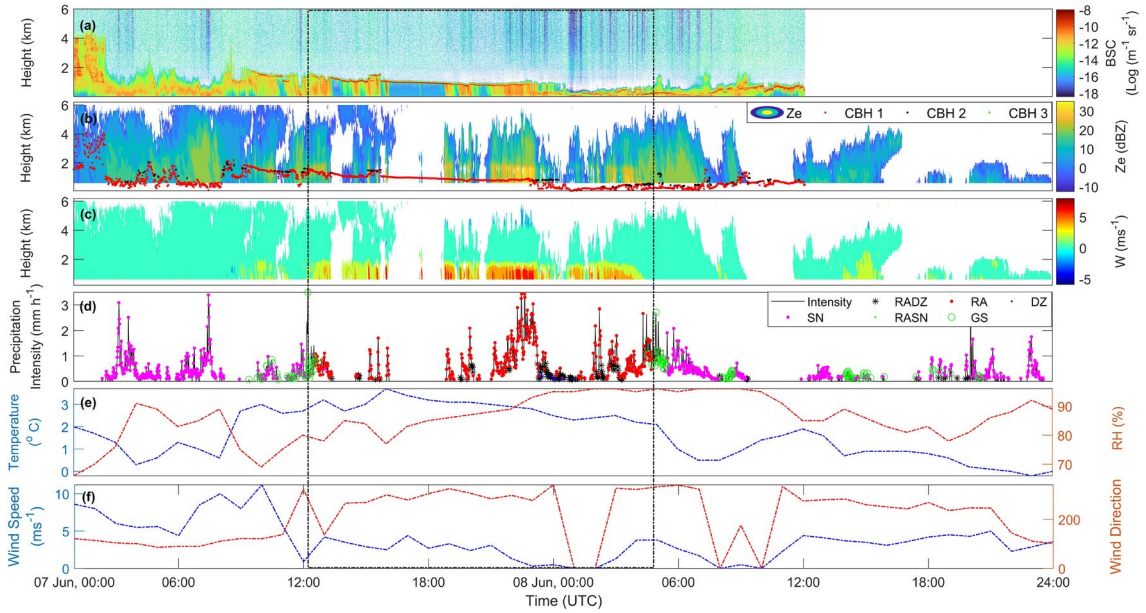

Fig. 9. Time series of vertical profiles: (a) BSC, (b) reflectivity (Ze) with CBH1 (red), CBH2 (blue), and CBH3 (green), (c) fall velocity (W) observed by ceilometer and MRR, respectively. Ground observations include (d) precipitation intensity from the disdrometer showing transitions from snow (SN, magenta) to rain (RA, red) and vice versa; (e) 2*m* temperature (blue dashed) and relative humidity (red dashed); and (f) mean wind speed (blue dashed) and wind direction (red dashed) for June 7^{th} - 8^{th}, 2020.

2 *km*, also known as the bright band in the precipitation profile[64,65]. During "Snow event-2", both BSC and CBH uplifted again as snowfall resumed, as observed in the datasets until 01:00 *UTC* on June 7^{th}. The radar reflectivity and fall velocity profiles were again uniform, but the profile extended only up to 4 *km*.

The atmospheric conditions in Figure 9(e-f) at ground level show temperature variation from 0 to $3.5^{o}C$, with the highest temperature recorded during the rainy phase. Similarly, relative humidity ranges from 65 to 95%, with the highest humidity observed in the rainy period, mirroring the ground temperature pattern. Initially, in the snow event-1, easterly winds near the surface blow at a velocity exceeding 5 ms^{-1}, transitioning to south-easterly then turns to northwesterly winds later in the rain event with reduced speed below 5 ms^{-1} as well as snow event-2.

Vertical atmospheric profiles from MWR in Figure 10(a-e) indicate notable atmospheric dynamics during transition from snowfall to rainfall and vice versa along with reflectivily. During the snow to rain transition, the vertical temperature profile exhibits a significant increment, particularly evident below $\sim$ 2 *km* altitude. This upward trend in temperature coincides with the establishment of a melting layer, identified at $\sim$ 2 *km* altitudes where temperature crosses the freezing point. Concurrently, there is a notable increase in both humidity and liquid water content within this layer, indicative of the phase transition from snow to rain and subsequent moisture release into the atmosphere.

The vertical profile of atmospheric conditions from the ERA5 hourly reanalysis dataset is also presented in Figure 10(f-j). Consistency between ERA5 and the MWR data is evident, particularly at the 800 *hPa* pressure level where temperatures exceed zero degrees Celsius, coinciding with high moisture as specific humidity. This mutual confirmation underscores the reliability of both datasets in depicting temperature variations.

Synoptic conditions during Snow event-1 at time instant A, as shown in Figure 11(A), the surface high-pressure system at the MSL brings cold southeasterly winds, with a small negative advection of temperature and moisture at 850 *hPa* level. High pressure system creates divergence at surface level due to increased speed of surface winds, leading to a near-surface downward wind motion from 900 *hPa*. These conditions, with an overall low temperature and moisture from a southeastern flow, create a favorable condition for sn

At time instant B during the rain event shown in Figure 11(B), the low-pressure system centered at the bottom of the Svalbard creates circular wind motion. This shifts the direction to easterly at the surface and brings warm, moist air from the east of the Svalbard, increasing surface temperatures above freezing and facilitating a transition to rain. At 850 *hPa*, warm air with high moisture advection becomes prominent, reinforcing the warming and eventually rainfall. At the 500 *hPa* level, a small convergence reduces upward wind motion, suppressing intense precipitation and favoring rainfall. At time instant C during rain Figure 11(C) shows the low level pressure system centered over Svalbard and the circular motion shifts the wind flow over location to a northward direction at surface with negative advection of moisture, but temperature still with positive advection leads to reduced rainfall intensity.

Snow event-2 presented in Figure 11(D) is characterized by a slightly weaker surface low-pressure system that is centered north of Svalbard and allows cold northerly winds to return, with low surface temperatures to

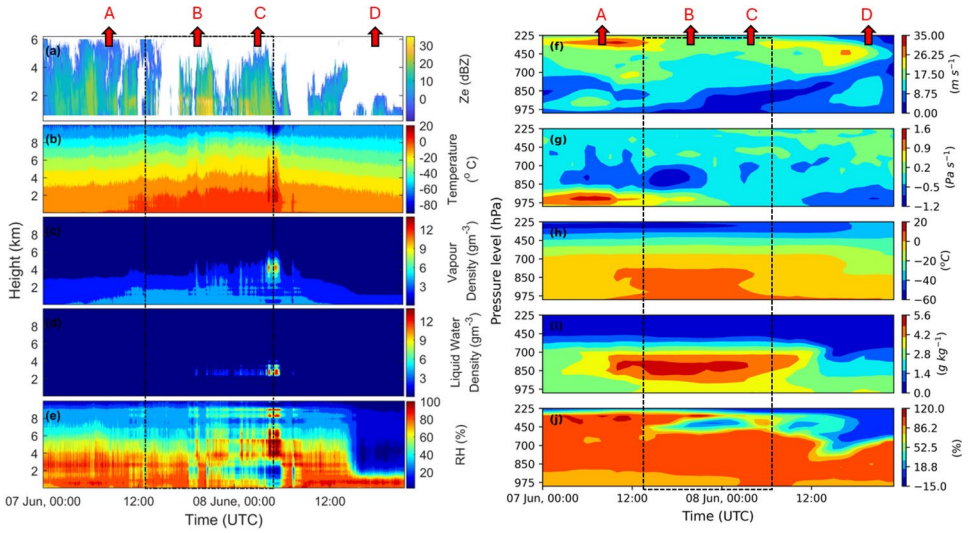

Fig. 10. Time series of (a) reflectivity (Ze) along with corresponding vertical atmospheric sounding from ground-based vertical profiler MWR: (b) temperature (^oC), (c) vapour density (gm^{-3}), (d) liquid water content (gm^{-3}), and (e) relative humidity (%). Vertical profile of atmospheric conditions based on ERA5 hourly reanalysis data: (f) horizontal wind speed (g) vertical velocity (h) temperature (^oC), (i) specific humidity (gkg^{-1}), and (j) relative humidity (%) during June 7^{th} - 8^{th}, 2020.

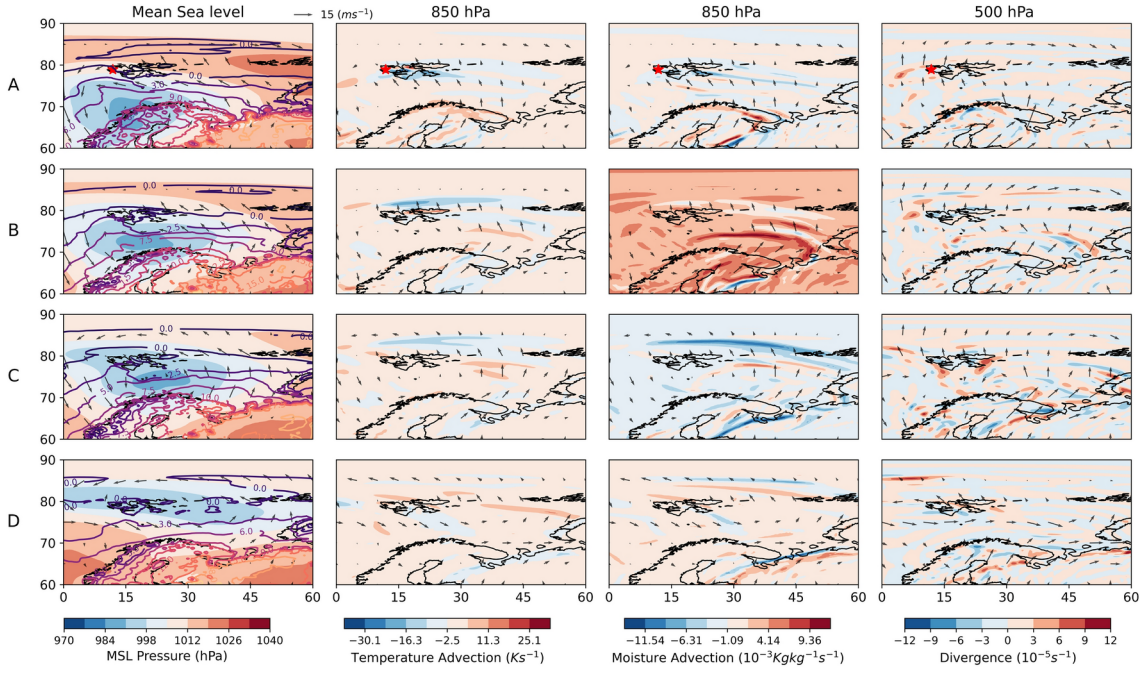

Fig. 11. Synoptic chart of MSL pressure with $2m$ level temperature contour line (column 1^{st}), temperature advection at 850 *hPa* level (column 2^{nd}), moisture advection at 850 *hPa* level (column 3^{rd}) and divergence at 500 *hPa* level (column 4^{th}) at four time instants during June 7^{th}-8^{th}, 2020, in rows: (A) June 7^{th} at 08:00 *UTC* ; (B)June 7^{th} at 20:00 *UTC*; (C)June 8^{th} on 04:00 *UTC*; and (D) June 8^{th} at 20:00 *UTC*.

sub-freezing levels. At 850 *hPa*, cold air advection resumes but is weaker compared to Snow event-1, resulting in limited moisture transport.

As per the vertical profile of temperature and specific humidity changes in the rain event between 700-850 *hPa* and the melting layer near ~ 2 *km* suggests the study of the spatio-temporal distribution of moisture pathways at 800 *hPa*. Figure 12(t-r)) present the temperature (t), vertical winds (w), specific humidity (q) and relative humidity (r). Figure 12(A-D)) Present this at four time instants A, B, C and D considering snow, rain, and their transition for time instants at 08:00, 20:00 *UTC* on June 7^{th}, and 04:00, 20:00 *UTC* on June, 8^{th} respectively. This

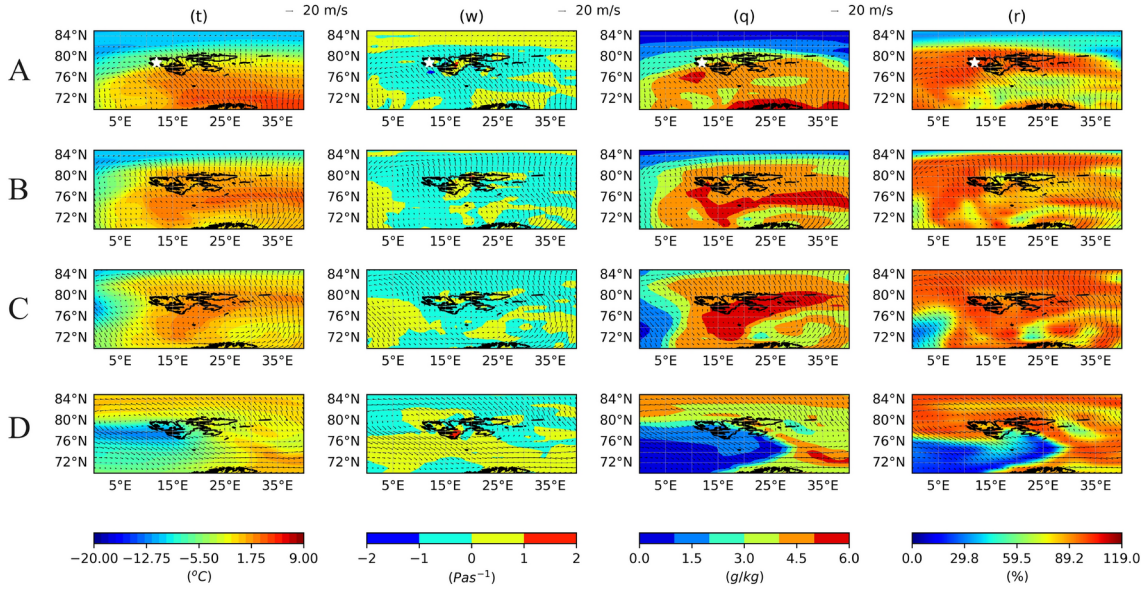

Fig. 12. Spatio-temporal distribution of atmospheric conditions with horizontal wind speed vectors at the 800 *hPa* pressure level, showing: (t) temperature (^oC), (w) vertical velocity (Pas^{-1}), (q) specific humidity (gkg^{-1}), and (r) relative humidity (%) at four time instants during June 7^{th}-8^{th}, 2020, in rows: (A) June 7^{th} at 08:00 *UTC* ; (B)June 7^{th} at 20:00 *UTC*; (C)June 8^{th} on 04:00 *UTC*; and (D) June 8^{th} at 20:00 *UTC*.

reveals a southeasterly wind flow originating from mid-latitude regions, which introduces warmer temperatures and moisture over Ny-Ålesund, denoted by the white star. The advection of high temperature and moisture content results in a melting layer and the transition of snowfall to rainfall, as shown in Figure 10(h-j). The horizontal wind speeds at times instant B and C during the rain period are notably high, around 20 ms^{-1} as shown in Figure 12(B-C).

At time instant C, the atmospheric conditions except wind pattern remain largely unchanged, as shown in Figure 12(C). It appears that the winds are circulating from the west of Svalbard, passing over the coastal region, and then returning as northwesterly direction accompanied by moderately upward velocity wind. The circular motion of this wind flow can be confirmed with HYSPLIT $24-hour$ wind back-trajectory from Figure S2 in the supporting file. These winds get slow and no longer carry as much moisture or warmth as they did previously, as shown in columns of Figure 12(t-r). As a result, when these returning winds hit the location at the time instant D in Figure 12(D), they arrive as dry winds with significantly lower moisture and temperature, as seen from vertical observation from Figure 10(b-e) and Figure 10(h-j). Integrated water vapour transport also describes the water flux presence during snow and rain at A-D time instants (see Figure S4 in the supporting file).

Normalized CFAD for radar reflectivity and fall velocity in Figure 13 provides additional insights into the microphysical evolution of precipitation during these three phases. In all three events, the CFAD of reflectivity reveals that precipitation exhibited reflectivity values ranging less than 10 *dBZ* at 6 *km* with a fall velocity below 1 ms^{-1}. However, as the precipitation reaches the ground, reflectivity increases linearly up to 20-25 *dBZ* and 1-2 ms^{-1} till $\sim$ 2 km. Below $\sim$ 2 *km* snow and rain both show different characteristics. Snow shows uniform reflectivity with approximately the same fall velocity observed below 2 *km* to ground as shown in Figure 13(a,c,d,f). In the rain profile, a sudden shift to the right was observed as reflectivity increased up to $\sim$40 *dBZ*, while fall velocity in this part increased up to 6 ms^{-1} (Figure 13(b,e)). This indicates that below 2 *km* snow falls uniformly while rain falls faster with bigger drops. This altitude level was identified as a melting layer, which was facilitated by hot-moist air mass as discussed above in atmospheric conditions in Figure 10.

Rain and snow in winter

To support and compare the findings from the above event of snow-rain transition in summer, this third event study from 2020 winter during November is 14^{th} - 16^{th} presented in Figure 14. This $52-hour$ long event shows different precipitation types at ground separated by black dotted lines highlighted in Figure 14(d). The first period, referred to as the "Rain event" (red dots), was characterized predominantly by rainfall observed at the ground from 08:20 *UTC* on November 14^{th} to 06:00 *UTC* on November 15^{th}. The other half, from 06:00 *UTC* on November 15^{th} to 11:00 *UTC* on November 16^{th}, was characterized as a "Snow event" . This indicates a shift from liquid to solid precipitation, including mixed snow as well as graupel. Snowfall occurs with higher intensity in this case compared to rainfall, unlike summer events. To investigate this precipitation transition, observations of BSC and CBH show cloud base height around $\sim$ 1 *km* during rain events with a high BSC. While cloud base height reduced during the transition to snow and later varies up to around 1 *km* with a comparably lower BSC, as shown in Figure 14(a-b). Figure 14(a-c) shows the MRR reflectivity (Ze) and fall velocity (W) profiles which stays up to 2 *km* for both snow and rain, however extends up to 5 *km* during the transition.

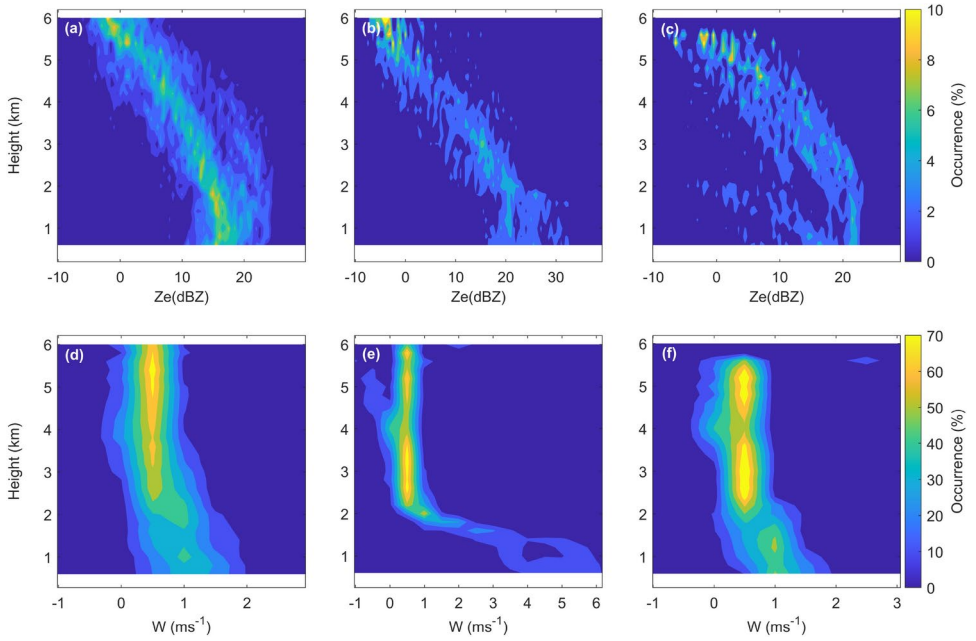

Fig. 13. Normalized (CFAD) for (a-c) reflectivity (Ze) and (d-f) fall velocity (W) for snow event-1, rain event and snow event-2, respectively, for June 07^{th}-08^{th}, 2020.

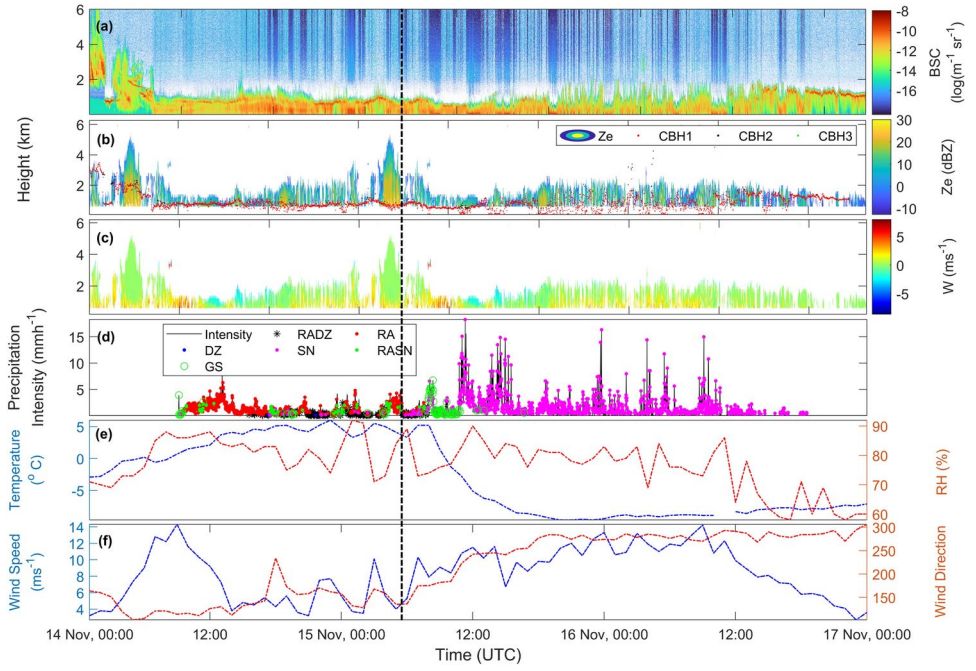

Fig. 14. Time series of vertical profiles: (a) BSC, (b) reflectivity (Ze) with CBH1 (red), CBH2 (blue), and CBH3 (green), (c) fall velocity (W) observed by ceilometer and MRR, respectively. Ground observations include (d) precipitation intensity from the disdrometer showing transitions from rain (RA, red) to snow (SN, magenta), (e) $2m$ temperature (blue dashed) and relative humidity (red dashed), and (f) mean wind speed (blue dashed) and wind direction (red dashed) for June 7^{th} - 8^{th}, 2020.

The near-surface conditions in Figure 14(e) show that the temperature rises above 0^oC at the start of the rain, reaching a peak of about 6^oC, which is the highest recorded during this precipitation event. As the precipitation shifts to snow, the temperature drops exponentially to $\sim$ -9^oC and remains relatively stable during the snow. The relative humidity varies from $\sim$ 70 to 90% during the rain and from $\sim$ 60 to 90% during the snow. In the beginning of rain, southeasterly winds near the surface blow at speeds of about 14 ms^{-1} as shown in Figure

14(f). These winds gradually shift to southerly directions with reduced speeds during the rain event and dropping to below 5 ms^{-1} during the transition to snow. During snowfall, the winds become more westerly and north-westerly, with higher speeds compared to the rainy phase.

Vertical atmospheric profiles from MWR, presented in Figure 15(a-e), clearly indicate the transition from rain to snow along with reflectivity. During the transition, temperature shows a significant shift from $10 - 20^oC$ to $\sim$ -20^oC particular below 2-3 *km* as shown in Figure 15(b). This temperature trend aligns closely with the vapour density, which extends up to 5 *km* during rain ($< 7\ gm^{-3}$) and near surface during snow ($< 2\ gm^{-3}$) as shown in Figure 15(c). Figure 15(d) presents the liquid water density ($\leq 14\ gm^{-3}$) observed between 2-3 *km* altitudes during rain. The presence of this liquid layer indicates the melting layer, which is less visible as a bright band in the MRR reflectivity. Consequently, relative humidity presented in Figure 15(d) peaks between 3-7 *km* during the rain, whereas below 2 *km* during the snow.

The vertical profile of the atmosphere from the ERA5 hourly reanalysis dataset is also presented in Figure 15(f-j). This event overall experienced low-level (< 850 *hPa*) slow winds ($\leq 15\ ms^{-1}$) in comparison with high-speed winds at high-level (> 850 *hPa*) as shown in Figure 15(f). During rain, vertical winds showed downward motion below ~ 850 *hPa*, slight upward motion between 850-500 *hPa*, and downward motion in the upper atmosphere. In comparison with rain event, snow event experience upward motion below 700 *hPa* and above 700 *hPa* shows similar downward motion as rain. Similar to the above two events, the strong correlation of MWR and ERA5 datasets confirms the reliability of ERA5 data for further use for spatio-temporal distribution of atmospheric parameters.

Figure 16 presents the synoptic conditions at various pressure levels (MSL, 850 *hPa*, 500 *hPa*) for the winter event at four time instants A, B, C and D representing rain, snow and their transitions on November 14^{th} at 00:00 *UTC* , November 15^{th} at 00:00 and 12:00 *UTC*, and November 16^{th} at 00:00 *UTC*. During initial time instant A in Figure 16(A), where no precipitation fall at ground, MSL pressure was high over Svalbard, brings the southeasterly cold winds to the surface. These winds at 850 *hPa* pressure level seen changed to southerly winds but negative moisture and temperature advection was observed results in no precipitation. In the next time instant B in Figure 16(B) during rain, the pressure over the location decreases, which changes the direction of winds to southwesterly. These winds bring warm moisture seen at 850 *hPa* levels results in positive advection of temperature and moisture and favor the rain. Time instant B is just before the transition to snow, which experiences slightly a negative advection of both moisture and advection. During time instant C in Figure 16(C) a low-pressure system moved to the north-west of Svalbard and brings northwesterly cold winds with limited moisture that made favorable conditions for the snowfall. Low pressure over Svalbard also induces surface level convergence, which causes a strong and sustained upward motion lasting over $24-hour$ from the surface up to the 700 *hPa* level (Figure 15(g)). This similar condition remains in time instant D in Figure 16(D) as the low-pressure system moved to the north and brings cold northern winds to make favorable conditions for snow.

Spatio-temporal distribution of moisture pathway at four time instants A, B, C and D representing rain and snow and their transitions is shown in the rows of Figure 17(t-r). This shows a southwesterly wind flow originating from lower latitudes, as confirmed by the HYSPLIT $24-hour$ back trajectory (see Figure S3 in the supplementary file). At the initial time instant A, Ny-Ålesund experiences cold temperatures with no significant

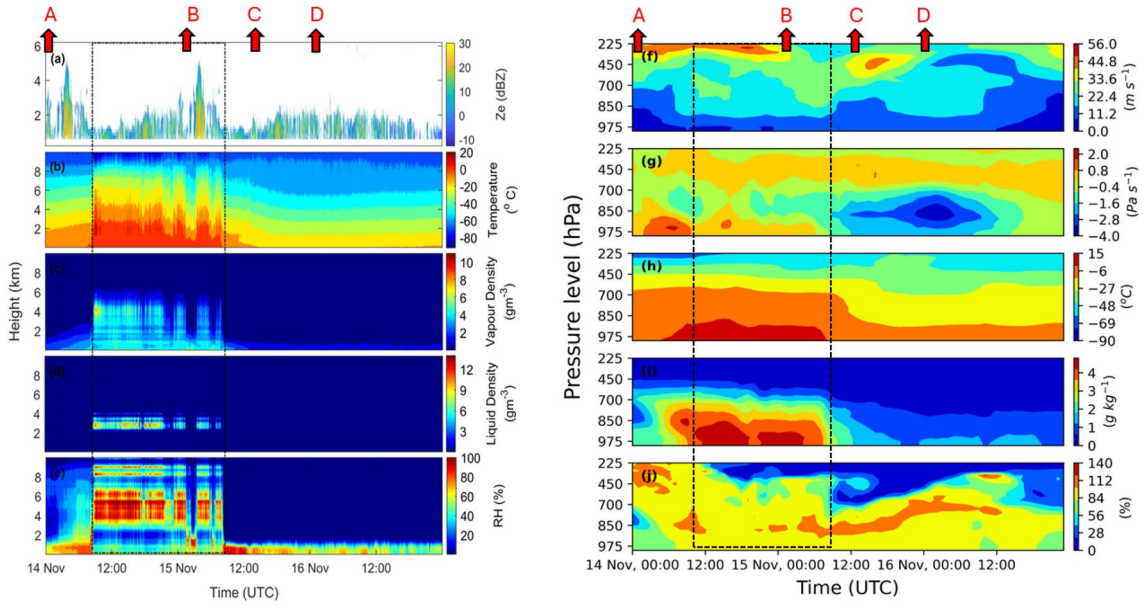

Fig. 15. Time series of (a) reflectivity (Ze) along with corresponding vertical atmospheric sounding from ground-based vertical profiler MWR: (b) temperature (^oC), (c) vapour density (gm^{-3}), (d) liquid water content (gm^{-3}), and (e) relative humidity (%). Vertical profile of atmospheric conditions based on ERA5 hourly reanalysis data: (f) horizontal wind speed (g) vertical velocity (h) temperature (^oC), (i) specific humidity (gkg^{-1}), and (j) relative humidity (%) for November 14^{th} - 16^{th} 2020.

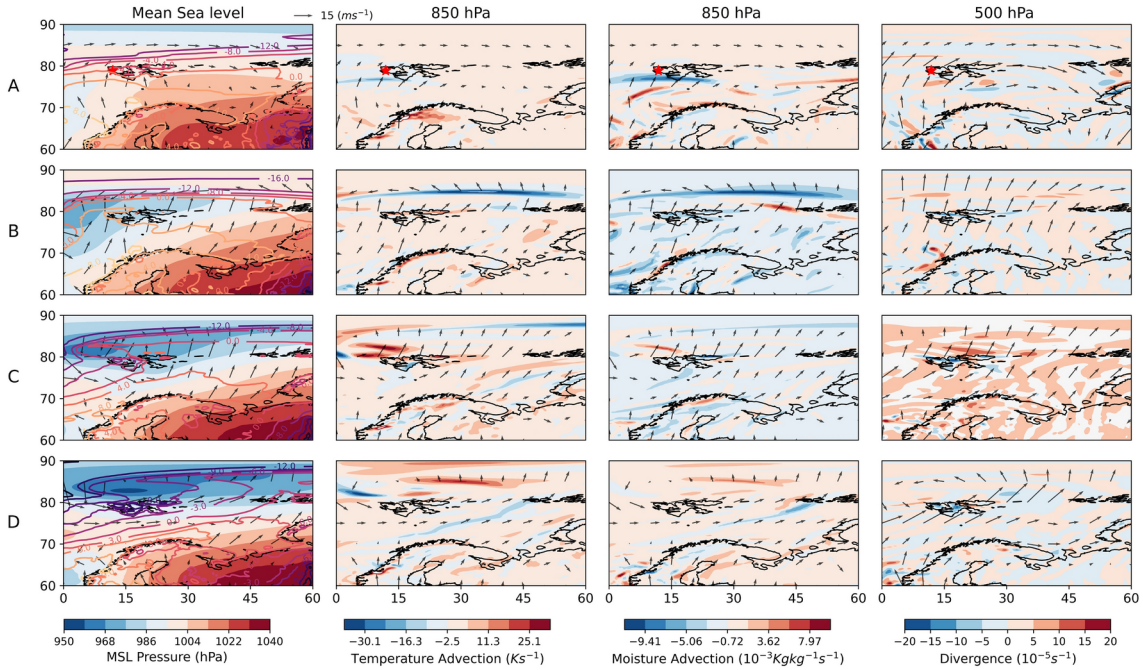

Fig. 16. Synoptic chart of MSL pressure with $2m$ level temperature contour line (column 1^{st}), temperature advection at 850 *hPa* level (column 2^{nd}), moisture advection at 850 *hPa* level (column 3^{rd}) and divergence at 500 *hPa* level (column 4^{th}) at four time instants during during November 14^{th}-16^{th}, 2020, in rows: (A) November 14^{th} at 00:00 *UTC* ; (B) November 15^{th} at 00:00 *UTC*; (C) November 15^{th} at 12:00 *UTC* and (D) November 16^{th} at 00:00 *UTC*.

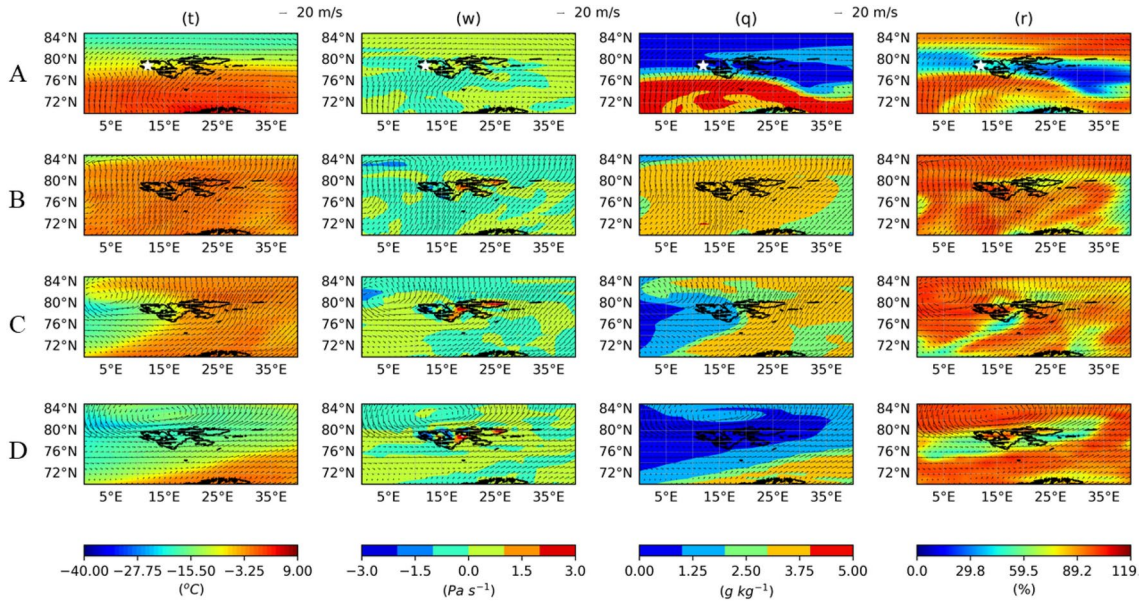

Fig. 17. Spatio-temporal distribution of atmospheric conditions with horizontal wind speed vectors at the 800 *hPa* pressure level, showing: (t) temperature (^oC), (w) vertical velocity (Pas^{-1}), (q) specific humidity (gkg^{-1}), and (r) relative humidity (%) at four time instants during November 14^{th}-16^{th}, 2020, in rows: (A) November 14^{th} at 00:00 *UTC* ; (B) November 15^{th} at 00:00 *UTC*; (C) November 15^{th} at 12:00 *UTC* and (D) November 16^{th} at 00:00 *UTC*.

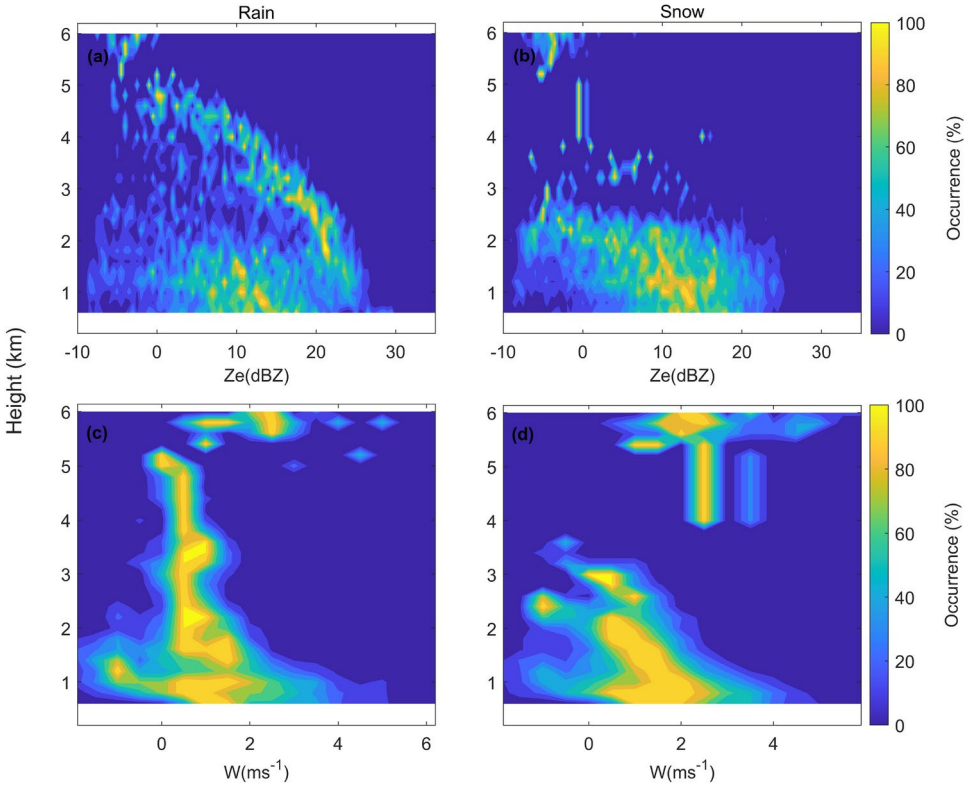

Fig. 18. Normalized (CFAD) for (a-b) reflectivity (Ze) and (c-d) fall velocity (W) for snow and graupel respectively for November 14^{th}-16^{th}, 2020.

specific humidity and low relative humidity, creating a no-precipitation scenario over the location, as shown in Figure 17(A). During time instant B, warmer temperatures and moisture are transported to Ny-Ålesund, as seen in Figure 17(B). This increase in temperature and moisture supports melting processes and raises relative humidity to its peak, leading to rain at the surface, as shown in Figure 14(d). During time instant C, the atmospheric flow shifts to a westerly direction, brings colder temperatures and reduced moisture, as shown in Figure 17(C), creating favorable conditions for snowfall. At the final time instant D, air masses from the northwesterly direction transport limited moisture, resulting in low relative humidity and a no-precipitation scenario at the surface, as seen in Figure 17(D). The wind direction can be confirmed with HYSPLIT $24-hour$ wind back-trajectory from Figure S3 in the supporting file. It shows the winds during rain originate from higher humidity southwest regions while for snow period it originate from low humidity northwest regions. Integrated water vapour transport also describes the water flux presence during rain and snow and no precipitation at A-D time instants (see Figure S5 in the supporting file).

The CFADs of radar reflectivity and fall velocity for both rain and snow events highlight distinct microphysical processes and vertical structures in winter. In the rain event, as shown in Figure 18(a), the reflectivity is concentrated up to 6 *km*, with values exceeding 25 *dBZ* predominantly below 2-3 *km*, which suggests the presence of moderate but smaller raindrops compared to the summer rain event, particularly below the melting layer. In contrast, the snow event shown in Figure 18(b) displays reflectivity primarily below 3 *km*, with moderate values ($\sim$20 *dBZ*) that maintain a more uniform vertical pattern. Looking at the fall velocity profiles, both events show similar characteristics. As shown in Figure 18(c-d), the maximum occurrence of fall velocities for both rain and snow is found between upto 5 ms^{-1} below 3 *km*. Both snow and rain also show negative velocities, indicating upward motion of droplets.

Discussion

This investigation presents three events studies over Ny-Ålesund (78.9^{o}N, 11.9^{o}E) illustrating a range of precipitation forms at the surface and analyzing their vertical and synoptic conditions. In-situ ground-based instruments were deployed for precipitation observations, with a MRR employed to capture the vertical profile of precipitation and a disdrometer used for measuring precipitation at the surface. A lidar ceilometer was used to observe cloud base height. To investigate the vertical synoptic conditions, ground-based MWR was used, and the profile was compared with the ERA5 reanalysis data profile, showing a strong correlation. Consequently, ERA5 data was further utilized to analyze spatio-temporal distribution. The analysis found that snow was the most dominant precipitation type, followed by rain and mixed-phase precipitation. The physical processes of the events are discussed here.

The first precipitation event from December 14^{th}-16^{th}, 2018, presents the atmospheric processes driving the transition between snow and graupel/small hail. The event began with comparably high pressure over the location, while a low-pressure system situated to the northwest of Svalbard. Wind circulation associated with this system brings south-westerly cold moist winds. This induced high relative humidity and a favorable condition for snow. The transition to graupel was marked by a shift of the low-pressure system to the north of Svalbard, which reduces the pressure at the location. Low surface pressure and above freezing level temperature create convergence, which leads to upward motion and induces instability. Similar conditions were also observed during the post-graupel hail[53]. Graupel was associated with an enhanced liquid water density profile at below freezing level temperature within mixed phase cloud between 1-3 *km* identified as supercooled water[47,66,67]. Instability caused by upward motion led to the collision of supercool water and ice crystals within mixed-phased cloud that results in the formation of graupel through riming process[55,58–60]. The subsequent return to snowfall was marked with the shift of low-pressure system to the northeast of Svalbard, brings northern cold winds. This results in reduction in temperature and moisture that results in low intensity precipitation. Graupel shows higher fall velocities, narrower reflectivity range compared to snow. This event highlights the presence of mixed-phase cloud over the Svalbard. A study also reported the presence of mixed-phase clouds over Svalbard through out the year with an average occurrence of 55%. This is higher than the average occurrence over Arctic which is 30% in winter and 50% rest of the year. It was found that mixed-phase clouds are especially located below 3 *km*, with a frequency of 90%, particularly during winter, spring and autumn. This is consistent with the observation of present study where mixed-phase clouds was found between 1-3 *km*.

The second event from summer 07^{th}-08^{th} June 2020 was divided into three distinct phases: snow event-1, rain event and snow event-2, each governed by unique atmospheric dynamics. The event started with high pressure over the study location and the low-pressure system centered to the south of Svalbard. This brings southeasterly cold winds that facilitate the transport of moisture and are favorable conditions for snowfall. The initial phase, snow event-1, was characterized by uniform radar reflectivity with fall velocity profiles extending upto 6 km. The shift of the low-pressure system over Svalbard brings southeasterly winds transporting warm, moist air, resulting in significant warming and moistening of the atmospheric column. Ground temperatures increased to 3.5^oC, accompanied by high relative humidity ∼95. The advection of warm, moist air above $\sim$ 8 50 *hPa* led to the formation of a melting layer between $\sim$ 2-3 *km* altitudes, characterized by enhanced liquid water density at this level. The melting layer was evident in MRR profiles, which showed increased reflectivity (up to 40 *dBZ*) and higher fall velocities (up to 6 ms^{-1}), consistent with phase transitions from solid to liquid precipitation. The final phase snow event-2, when the low-pressure system centered to north Svalbard, brings northwesterly winds but with reduced moisture and temperature supply led surface temperatures drop below freezing. Radar reflectivity and fall velocity profiles indicated a reduction in the vertical extent to 4 *km* with uniform vertical evolution. A study on Svalbard precipitation also highlights that heavy precipitation and rain events are driven by strong poleward flows transporting water vapor from warmer regions[68]. These winds enhance downwelling longwave radiation, raising surface temperatures and intensifying precipitation, especially during cyclonic conditions influenced by such flows[53,69].

The third rain-snow winter event, observed from November 14^{th} to 16^{th}, 2020, provides a contrasting scenario to the summer event in terms of synoptic conditions and microphysical processes. The event began with rainfall and transitioned to snow over a $52-hour$ period. During the rain phase, a low-pressure system located to the west of Svalbard that facilitates a southwesterly flow, transporting warm and moist air over the location. This warm-moist advection led to temperatures rise above freezing level, resulting in rainfall. Enhanced liquid density during the rain phase indicates the melting layer between ∼2-3 *km*. As the low-pressure system moved north of Svalbard, the surface wind shifted to a northwesterly direction, bringing colder air into the region. This cold air reduced the temperature profile significantly, dropping below freezing level, which led to the transition from rain to snow. The MRR profile indicates that during the rain event, reflectivity extends up to 5-6 *km*, with values above 25 *dBZ* predominantly observed below 3 *km* lower than the summer event. In contrast, during the snow event, the reflectivity profile is mainly confined below 3 *km*. Fall velocity profile of both snow and rain indicates the upward motion of droplets.

Conclusion

The present study highlights the role of microphysical and dynamical processes that result in different forms of precipitation over Ny-Ålesund in the Arctic. In conclusion, the present study highlights the following salient points based on the event studied:

- A distinct vertical profile of snow, rain and graupel is observed, which could be useful to differentiate the type of precipitation from remote sensing data.
- The melting layer/ bright band is formed between $\sim$ 2-3 *km* above the ground level indicating the phase change in that region. The vertical evolution of snow was found to be uniform as compared to rain, where reflectivity and fall velocity increase toward the surface.
- The collision of the supercooled water with ice crystals via the riming process within mixed-phased cloud leads to the formation of graupel. The upward motion was found to be a significant factor in the process. The graupel was found to be associated with higher fall velocity and narrower reflectivity range as compared to snow.
- The transition between snow and rain/graupel is mostly influenced by tropospheric conditions more than surface temperature. For the cases presented here, it is observed that Northwesterly and Northeasterly cold moist winds favor snowfall, whereas the poleward warm-moist air masses promote rainfall/ graupel at the study location.

This study also highlights the microphysical evolution of various precipitation types across different altitudes. However, further in-depth research is required to generalize these findings for Arctic precipitation. This knowledge is essential for improving quantitative precipitation estimation from both space-borne and ground-based radars, which will be crucial for developing numerical weather prediction (NWP) models for more accurate forecasting.

Data availability

The global ERA5 reanalysis datasets and surface-level meteorological data from the Norwegian Polar Institute used in this study are freely available at https://cds.climate.copernicus.eu/ and https://seklima.met.no/, respectiv ely. The in-situ observed precipitation and synoptic datasets are available upon request from the corresponding author, S.D.

Received: 17 September 2024; Accepted: 6 January 2025
Published online: 24 January 2025

References

1. Solomon, S., Qin, D., Manning, M., Averyt, K. & Marquis, M. *Climate change 2007-the physical science basis: Working group I contribution to the fourth assessment report of the IPCC* (Cambridge university press) https://www.ipcc.ch/site/assets/uploads/2020/02/ar4-wg1-sum_vol_en.pdf (2007)
2. Hassol, S. *Impacts of a warming Arctic-Arctic climate impact assessment* (Cambridge University Press, 2004).
3. Macdonald, R. W., Harner, T. & Fyfe, J. Recent climate change in the Arctic and its impact on contaminant pathways and interpretation of temporal trend data. *Science of the total environment* **342**, 5–86 (2005).
4. Ernakovich, J. G. et al. Predicted responses of arctic and alpine ecosystems to altered seasonality under climate change. *Global Change Biology* **20**, 3256–3269 (2014).
5. Bintanja, R. & Selten, F. Future increases in Arctic precipitation linked to local evaporation and sea-ice retreat. *Nature* **509**, 479–482 (2014).
6. Dou, T. & Xiao, C. *The Impacts of Atmospheric Ice Reduction in the Lower Troposphere on the Snow and Ice Processes over the Arctic* tech. rep. (Copernicus Meetings, 2023).
7. Bintanja, R. & Andry, O. Towards a rain-dominated Arctic. *Nature Climate Change* **7**, 263–267 (2017).
8. Athulya, R., Nuncio, M., Chatterjee, S. & Vidya, P. Characteristics of mean and extreme precipitation in Ny Ålesund. *Arctic. Atmospheric Research* **295**, 106989 (2023).
9. Henderson, G. R. et al. Local and remote atmospheric circulation drivers of Arctic change: A review. *Frontiers in Earth Science* **9**, 709896 (2021).
10. Gultepe, I., Isaac, G., Williams, A., Marcotte, D. & Strawbridge, K. Turbulent heat fluxes over leads and polynyas, and their effects on arctic clouds during FIRE. ACE: Aircraft observations for April 1998. *Atmosphere-Ocean* **41,** 15–34 (2003).
11. Das, S. & Maitra, A. Vertical profile of rain: Ka band radar observations at tropical locations. *Journal of Hydrology* **534,** 31–41. 0022-1694. https://www.sciencedirect.com/science/article/pii/S002216941501001X (2016).
12. Das, S., Shukla, A.K. & Maitra, A. Investigation of vertical profile of rain microstructure at Ahmedabad in Indian tropical region. *Advances in Space Research* **45,** 1235–1243. 0273-1177. https://www.sciencedirect.com/science/article/pii/S0273117710000219 (2010).
13. Durán-Alarcón, C. et al. The vertical structure of precipitation at two stations in East Antarctica derived from micro rain radars. *The Cryosphere* **13**, 247–264 (2019).
14. Alárcon, C.D. *Ground-based remote sensing of Antarctic and Alpine solid precipitation* PhD thesis (Université Grenoble Alpes, 2019).
15. Serreze, M.C. et al. The large-scale energy budget of the Arctic. *Journal of Geophysical Research: Atmospheres* **112** (2007).
16. Serreze, M. C., Barrett, A., Stroeve, J., Kindig, D. & Holland, M. The emergence of surface-based Arctic amplification. *The cryosphere* **3**, 11–19 (2009).
17. Maturilli, M. & Kayser, M. Arctic warming, moisture increase and circulation changes observed in the Ny-Ålesund homogenized radiosonde record. *Theoretical and Applied Climatology* **130**, 1–17 (2017).
18. Przybylak, R., Sadourny, R. & Mysak, L.A. The climate of the Arctic (2003).
19. Serreze, M. C., Crawford, A. D. & Barrett, A. P. Extreme daily precipitation events at Spitsbergen, an Arctic Island. *International Journal of Climatology* **35**, 4574–4588 (2015).
20. Dahlke, S., Solbès, A. & Maturilli, M. Cold air outbreaks in Fram Strait: Climatology, trends, and observations during an extreme season in 2020. *Journal of Geophysical Research: Atmospheres* **127,** e2021JD035741 (2022).
21. Nuttall, M. *Encyclopedia of the Arctic* (Routledge, 2005).
22. Hanssen-Bauer, I. & Førland, E. Long-term trends in precipitation and temperature in the Norwegian Arctic: can they be explained by changes in atmospheric circulation patterns?. *Climate Research* **10**, 143–153 (1998).
23. Sepp, M. & Jaagus, J. Changes in the activity and tracks of Arctic cyclones. *Climatic Change* **105**, 577–595 (2011).
24. Førland, G. M., Liang, Y., Kvalheim, O. M., Høiland, H. & Chazy, A. Associative behavior of benzyl alcohol in carbon tetrachloride solutions. *The Journal of Physical Chemistry B* **101**, 6960–6969 (1997).
25. Førland, E. J. & Hanssen-Bauer, I. Increased precipitation in the Norwegian Arctic: true or false?. *Climatic change* **46**, 485–509 (2000).
26. Araźny, A., Przybylak, R. & Kejna, M. The influence of atmospheric circulation on mean and extreme weather conditions on Kaffiøyra (NW Spitsbergen, Svalbard Archipelago) in the summer seasons 1975–2015. *Frontiers in Environmental Science* **10**, 867106 (2022).
27. Hunter, J. D. Matplotlib: A 2D graphics environment. *Computing in Science & Engineering* **9**, 90–95 (2007).
28. Norwegian Center for Climate Services. *The Norwegian Meteorological Institute (MET Norway)*[SPACE]https://seklima.met.no/. Retrieved June 5, 2024.
29. Hersbach, H. et al. *ERA5 hourly data on pressure levels from 1940 to present* Copernicus Climate Change Service (C3S) Climate Data Store (CDS). Accessed on 05-06-2024. 2023.
30. Stein, A.F. et al. NOAA's HYSPLIT Atmospheric Transport and Dispersion Modeling System. *Bulletin of the American Meteorological Society* **96,** 2059–2077. https://journals.ametsoc.org/view/journals/bams/96/12/bams-d-14-00110.1.xml (2015).
31. Maahn, M. & Kollias, P. Improved Micro Rain Radar snow measurements using Doppler spectra post-processing. *Atmospheric Measurement Techniques* **5**, 2661–2673 (2012).
32. *OTT Parsivel-2 disdrometer manual* 2023. https://psl.noaa.gov/data/obs/instruments/OpticalDisdrometer.pdf
33. Löffler-Mang, M. & Joss, J. An optical disdrometer for measuring size and velocity of hydrometeors. *Journal of Atmospheric and Oceanic Technology* **17**, 130–139 (2000).

34. Oyj, V. *Ceilometer CL51 Datasheet (B210861EN-G.1)*[SPACE]https://docs.vaisala.com/v/u/B210861EN-G.1/en-US. Retrieved June 6, 2024. 2022.
35. Maturilli, M. & Ebell, K. Twenty-five years of cloud base height measurements by ceilometer in Ny-Ålesund, Svalbard. *Earth System Science Data* **10,** 1451–1456. https://essd.copernicus.org/articles/10/1451/2018/ (2018).
36. Solheim, F. et al. Radiometric profiling of temperature, water vapor and cloud liquid water using various inversion methods. *Radio Science* **33**, 393–404 (1998).
37. Güldner, J. & Spänkuch, D. Remote sensing of the thermodynamic state of the atmospheric boundary layer by ground-based microwave radiometry. *Journal of Atmospheric and Oceanic Technology* **18**, 925–933 (2001).
38. Solheim, F., Godwin, J. R. & Ware, R. Passive ground-based remote sensing of atmospheric temperature, water vapor, and cloud liquid water profiles by a frequency synthesized microwave radiometer. *Meteorologische zeitschrift-berlin* **7**, 370–376 (1998).
39. Knupp, K. et al. Ground-based passive microwave profiling during dynamic weather conditions. *Journal of Atmospheric and Oceanic Technology* **26**, 1057–1073 (2009).
40. Kneifel, S., Maahn, M., Peters, G. & Simmer, C. Observation of snowfall with a low-power FM-CW K-band radar (Micro Rain Radar). *Meteorology and Atmospheric Physics* **113**, 75–87 (2011).
41. Jarraud, M. *Guide to meteorological instruments and methods of observation (WMO-No. 8), World Meteorological Organisation* 2008.
42. Dorff, H., Konow, H., Schemann, V. & Ament, F. Observability of moisture transport divergence in Arctic atmospheric rivers by dropsondes. *Atmospheric Chemistry and Physics* **24,** 8771–8795. https://acp.copernicus.org/articles/24/8771/2024/ (2024).
43. Asutosh, A., Chatterjee, S., Subeesh, M., Radhakrishnan, A. & Murukesh, N. Observation of Cloud Base Height and Precipitation Characteristics at a Polar Site Ny-Ålesund, Svalbard Using Ground-Based Remote Sensing and Model Reanalysis. *Remote Sensing* **13.** 2072-4292. https://www.mdpi.com/2072-4292/13/14/2808 (2021).
44. Ebell, K., Nomokonova, T., Maturilli, M. & Ritter, C. Radiative effect of clouds at Ny-Ålesund, Svalbard, as inferred from ground-based remote sensing observations. *Journal of Applied Meteorology and Climatology* **59**, 3–22 (2020).
45. Shupe, M. D. & Intrieri, J. M. Cloud radiative forcing of the Arctic surface: The influence of cloud properties, surface albedo, and solar zenith angle. *Journal of climate* **17**, 616–628 (2004).
46. Strangeways, I. *Precipitation: theory, measurement and distribution* (Cambridge University Press, 2006).
47. Angell, C.A. in *Water and Aqueous Solutions at Subzero Temperatures* (ed Franks, F.) 1–81 (Springer US, Boston, MA, 1982). ISBN: 978-1-4757-6952-4. https://doi.org/10.1007/978-1-4757-6952-4_1
48. Jones, R. F. Water and Ice in the Atmosphere. *The Journal of the Royal Aeronautical Society* **63**, 465–473 (1959).
49. Riley, J. in *37th Aerospace Sciences Meeting and Exhibit*. eprint: https://doi.org/10.2514/6.1999-99
50. Hallett, J. & Isaac, G.A. Aircraft Icing in Glaciated and Mixed Phase Clouds. *Journal of Aircraft* **45,** 2120–2130. eprint: https://doi.org/10.2514/1.37596. (2008).
51. Intrieri, J., Shupe, M., Uttal, T. & McCarty, B. An annual cycle of Arctic cloud characteristics observed by radar and lidar at SHEBA. *Journal of Geophysical Research: Oceans* **107,** SHE–5 (2002).
52. Heymsfield, A. J., Miloshevich, L. M., Slingo, A., Sassen, K. & Starr, D. O. An observational and theoretical study of highly supercooled altocumulus. *Journal of Atmospheric Sciences* **48**, 923–945 (1991).
53. Nuncio, M. et al. Hails in Ny Alesund, Svalbard-atmospheric vertical structure and dependence on circulation. *Natural Hazards* **117**, 1365–1380 (2023).
54. Gultepe, I., Rabin, R., Ware, R. & Pavolonis, M. in *Advances in Geophysics* 147–210 (Elsevier, 2016).
55. Reinking, R.F. Formation of Graupel. *Journal of Applied Meteorology (1962-1982)* **14,** 745–754. 00218952, 2163534X. http://www.jstor.org/stable/26176595 (2024) (1975).
56. Pflaum, J. & Pruppacher, H. A wind tunnel investigation of the growth of graupel initiated from frozen drops. *Journal of Atmospheric Sciences* **36**, 680–689 (1979).
57. Khain, A. P. & Sednev, I. Simulation of precipitation formation in the Eastern Mediterranean coastal zone using a spectral microphysics cloud ensemble model. *Atmospheric Research* **43**, 77–110 (1996).
58. Khain, A., Pokrovsky, A. & Sednev, I. Some effects of cloud-aerosol interaction on cloud microphysics structure and precipitation formation: Numerical experiments with a spectral microphysics cloud ensemble model. *Atmospheric research* **52**, 195–220 (1999).
59. Wang, P.K. & Kubicek, A. Flow fields of graupel falling in air. *Atmospheric Research* **124,** 158–169. 0169-8095. https://www.sciencedirect.com/science/article/pii/S0169809513000148 (2013).
60. Arenberg, D. L. The formation of small hail and snow pellets. *Bulletin of the American Meteorological Society* **22**, 113–116 (1941).
61. Battan, L. *1973. Radar Observation of the Atmosphere* 1973.
62. Ryzhkov, A. & Krause, J. New polarimetric radar algorithm for melting-layer detection and determination of its height. *Journal of Atmospheric and Oceanic Technology* **39**, 529–543 (2022).
63. Zhang, J., Langston, C. & Howard, K. Brightband identification based on vertical profiles of reflectivity from the WSR-88D. *Journal of Atmospheric and Oceanic Technology* **25**, 1859–1872 (2008).
64. Klaassen, W. Radar observations and simulation of the melting layer of precipitation. *Journal of Atmospheric Sciences* **45**, 3741–3753 (1988).
65. Willis, P. T. & Heymsfield, A. J. Structure of the melting layer in mesoscale convective system stratiform precipitation. *Journal of Atmospheric Sciences* **46**, 2008–2025 (1989).
66. Shupe, M. D., Matrosov, S. Y. & Uttal, T. Arctic mixed-phase cloud properties derived from surface-based sensors at SHEBA. *Journal of the atmospheric sciences* **63**, 697–711 (2006).
67. Mioche, G., Jourdan, O., Ceccaldi, M. & Delanoë, J. Variability of mixed-phase clouds in the Arctic with a focus on the Svalbard region: a study based on spaceborne active remote sensing. *Atmospheric Chemistry and Physics* **15**, 2445–2461 (2015).
68. Viceto, C. et al. Atmospheric rivers and associated precipitation patterns during the ACLOUD and PASCAL campaigns near Svalbard (May-June 2017): case studies using observations, reanalyses, and a regional climate model. *Atmospheric Chemistry and Physics* **22**, 441–463 (2022).
69. Dobler, A., Lutz, J., Landgren, O. & Haugen, J.E. Circulation Specific Precipitation Patterns over Svalbard and Projected Future Changes. *Atmosphere* **11,** 1378– (2020).

Acknowledgements

The authors acknowledge the Ministry of Earth Sciences, Govt. of India, and the Director of ESSO - NCPOR for their valuable support throughout this study. The NCPOR contribution no is J-52/2024-25. First author (LS) is thankful to CSIR for the fellowship. One of the authors (SD) acknowledges the financial support provided by SERB (Grant: CRG/2022/006986) and MoES (MoES/16/4/2021-RDESS/NARM-4). The authors are also thankful to ECMWF for providing ERA5 datasets and Norway Norsk Klimaservicesenter (met.no) for surface observation at Ny-Ålesund. The authors thank two anonymous reviewers and the editor for their valuable comments.

Author contributions

L.S. performed formal analysis, conceptualization, developed the methodology, investigation, interpretation,

and prepared the main manuscript. S.D. conceptualized the study, developed the methodology, provided supervision, and contributed to writing, reviewing, and editing. N.M. curated the data, provided supervision, and contributed to writing, reviewing, and editing.

Additional information

Supplementary Information The online version contains supplementary material available at https://doi.org/10.1038/s41598-025-85833-2.

Correspondence and requests for materials should be addressed to S.D.

Reprints and permissions information is available at www.nature.com/reprints.

Publisher's note Springer Nature remains neutral with regard to jurisdictional claims in published maps and institutional affiliations.